Prediction of traction forces of motile cells

Clément Roux, Alain Duperray, Valérie Laurent, Richard Michel, Valentina Peschetola, Claude Verdier, Jocelyn Etienne

To cite this version:

Clément Roux, Alain Duperray, Valérie Laurent, Richard Michel, Valentina Peschetola, et al.. Prediction of traction forces of motile cells. Interface Focus, 2016, Theme issue 'Coupling geometric partial differential equations with physics for cell morphology, motility and pattern formation' organized by Rudolf Leube, Anotida Madvamuse, Rudolf Merkel and Hans Othmer, 6 (5), 10.1098/rsfs.2016.0042 . hal-01391213

HAL Id: hal-01391213
https://hal.univ-grenoble-alpes.fr/hal-01391213v1

Submitted on 4 Nov 2016

Prediction of traction forces of motile cells

Clément Roux[1,2] Alain Duperray[3,4]
Valérie M. Laurent[1,2] Richard Michel[1,2]
Valentina Peschetola[1,2] Claude Verdier[1,2]
Jocelyn Étienne[1,2,*]

1. Univ. Grenoble Alpes, Laboratoire interdisciplinaire de physique (LIPHY), F-38000 Grenoble,
2. CNRS, Laboratoire interdisciplinaire de physique (LIPHY), F-38000 Grenoble,
3. Univ. Grenoble Alpes, IAB, F-38000 Grenoble, France,
4. INSERM, IAB, F-38000 Grenoble, France,
* To whom correspondence should be sent, Jocelyn.Etienne@univ-grenoble-alpes.fr

When crawling on a flat substrate, living cells exert forces on it via adhesive contacts, enabling them to build up tension within their cytoskeleton and to change shape. The measurement of these forces has been made possible by traction force microscopy (TFM), a technique which has allowed us to obtain time-resolved traction force maps during cell migration. This cell "footprint" is however not sufficient in order to understand the details of the mechanics of migration, that is, how cytoskeletal elements (respectively, adhesion complexes) are put under tension and reinforce or deform (respectively, mature and/or unbind) as a result. In a recent paper, we have validated a rheological model of actomyosin linking tension, deformation and myosin activity. Here, we complement this model with tentative models of the mechanics of adhesion and explore how closely these models can predict the traction forces that we recover from experimental measurements during cell migration. The resulting mathematical problem is a PDE set on the experimentally observed domain, which we solve using a finite-element approach.

1 Introduction

During immunoresponse and cancer metastasis formation, cells crawl on the blood vessel wall [1]. This type of cell motion has been reproduced in vitro [2] and has been the subject of many modelling studies [3, 4, 5].

Since inertial effects and body forces are vanishingly small in this process, all forces are instantaneously balanced in the system and in particular, the resultant of the traction forces that the cell exerts on its environment has to be zero. The motion of the crawling cell is thus necessarily driven by its deformation, as the cell changes shape both by growth and shrinkage due to (de)polymerisation at its leading edges [6, 7]. and simultaneously as actin cytoskeleton undergoes a persistent centripetal deformation, called retrograde flow [8, 9, 10], In order to result in a net displacement of the cell with respect to its surroundings, forces need to be transmitted to it. Although fluid drag and non-specific interactions with the solid substrate are present, most of the stress is transmitted via specific adhesion interaction between ligands present on the surface of the substrate and transmembrane receptors which are bound to the actin cytoskeleton [11].

The mechanical models attempting to explain cell migration from the dynamics of its microstructure are thus focusing on the dynamics of actomyosin and adhesion complexes [12]. Important modelling efforts have been made since in order to understand the initiation and maintenance of motility [13, 14, 15, 16, 17]. These works are using the simple and stable shape of keratocyte cells, or a one-dimensional simplification. While this allows for a fine understanding of possible detailed mechanisms of motility and is based on the same mechanisms of actin (de)polymerisation and myosin-driven retrograde flow, the migration of keratocyte does not present the cycle of events observed in most other cell types during migration [18]. Moreover, altough these models are shown to fit experimental results, in general they have not yet been exploited in a systematic manner. Indeed, quantitative prediction of cell dynamics and exerted forces is only at its beginning [19, 20, 21]: while fitting models remains in all cases necessary to acquire a minimal set of parameters from a subset of the experiments available, these recent papers are additionally predictive of other experimental conditions for which no further adjustment is done.

Here we combine the prediction of a simple yet quantitatively validated rheological model of actomyosin [21] with a nonlinear model of cell adhesion adapted from [16] and simulate it on the actual geometry of cells tracked while crawling. Monitoring the deformation of the substrate during the experiment [22] and a traction force microscopy (TFM) method [23, 24, 25, 26, 27] allows us to compute independently the traction forces that the cell exerts on the substrate, to which the predicted traction fields can be compared. The number of adjustable parameters is reduced to a minimum (two for the linear model, four for the nonlinear adhesion model) and the robustness of the parameter choice is assessed in a systematic way and the preditive capability of the model is tested over different cell migration events and cell types.

Experimental observations in the literature give consistent pictures of two different scales: the microscopic scale, at which the dynamics of the relevant molecules are well described (actin, actin-binding molecules and adhesion molecules), and the mesoscopic scale of the cell itself. Our approach is to write a mechanical model based on the microscale knowledge, and investigate how these microscale dynamics yield the emergent mesoscale behaviours that are observed. In a previous paper [21], we have successfully used this type of approach and validated quantitatively at the mesoscale a rheological constitutive law based on a microscale model of actomyosin dynamics.

However, the setup used in that work did not require a precise model of the mechanics of cell adhesion, whereas this is needed here in order to address cell crawling. Cell adhesion models of graded complexity have been introduced by many authors [28, 29, 16]. Our numerical resolution procedure and quantitative comparison with experimental data will allow us to investigate which of these models match best the observations.

2 Mesoscale experimental observations

We observe cancer cells from two different cancer cell lines (T24 and RT112 cell lines) which are crawling on a relatively stiff gel, $E = 10\,\mathrm{kPa}$. Our experimental observations, traction force recovery and the relevant other observations in the literature are described briefly in the appendices 6.1 and 6.2, and at length in [27]. Here we summarise only some salliant features that will need to be accounted for by the model predictions.

When plated on the gel, T24 cells assume an elongated and digitated shape, while RT112 cells have a rounded shape, figure 1. For both lines, as well as in all other observations in the literature, the traction forces they exert are minimal close to their geometric center and increases distally (close to the cell edge). The tractions are oriented approximately along the normal to the cell edge, pointing inwards, figure 1*c*. The rate of increase of traction force along an imaginary line from cell centroid to cell edge is greater when the cell edge is close to centroid, but the intensity of traction goes generally to much larger values close to the part of cell edges which are more distal (farther away from centroid). In many instances, the maxima of the traction field are not situated right at the cell edge but somewhat proximal (inwards) from it, and tractions can be vanishingly small at the edge. In what follows, we will attempt to link these observations with both the phenomenology of adhesion complexes (as is done e.g. in [30]) and with the mechanics of the cytoskeleton.

3 Microscale-based mechanical model

It is well established experimentally that the mechanical properties of crawling cells are controlled by their actin structures and the proteins that bind to actin [2]. Although other cytoskeletal components have a smaller contribution in the mechanical balance, we will neglect them in what follows. Above a timescale between 0.1 to 10 s, the pressure in the cytosol equilibrates [31] and the poroelastic behaviour of the cell becomes negligible. Thus the variable of interest is the stress tensor $\boldsymbol{\sigma}^{\mathrm{3D}}$ in the actin meshwork (and its strain and rate-of-strain tensors $\boldsymbol{\varepsilon}^{\mathrm{3D}}$ and $\dot{\boldsymbol{\varepsilon}}^{\mathrm{3D}}$) at any position in the cell. In the absence of inertia and at sufficiently long timescale, the force balance writes

$$\nabla \cdot \boldsymbol{\sigma}^{\mathrm{3D}} = \boldsymbol{F} \quad \text{in } \Omega^{\mathrm{3D}}$$

where $\boldsymbol{F}$ are bulk forces, discussed below. This internal stress of the actin needs to be balanced at the boundaries of the actin meshwork: thus the actin stress

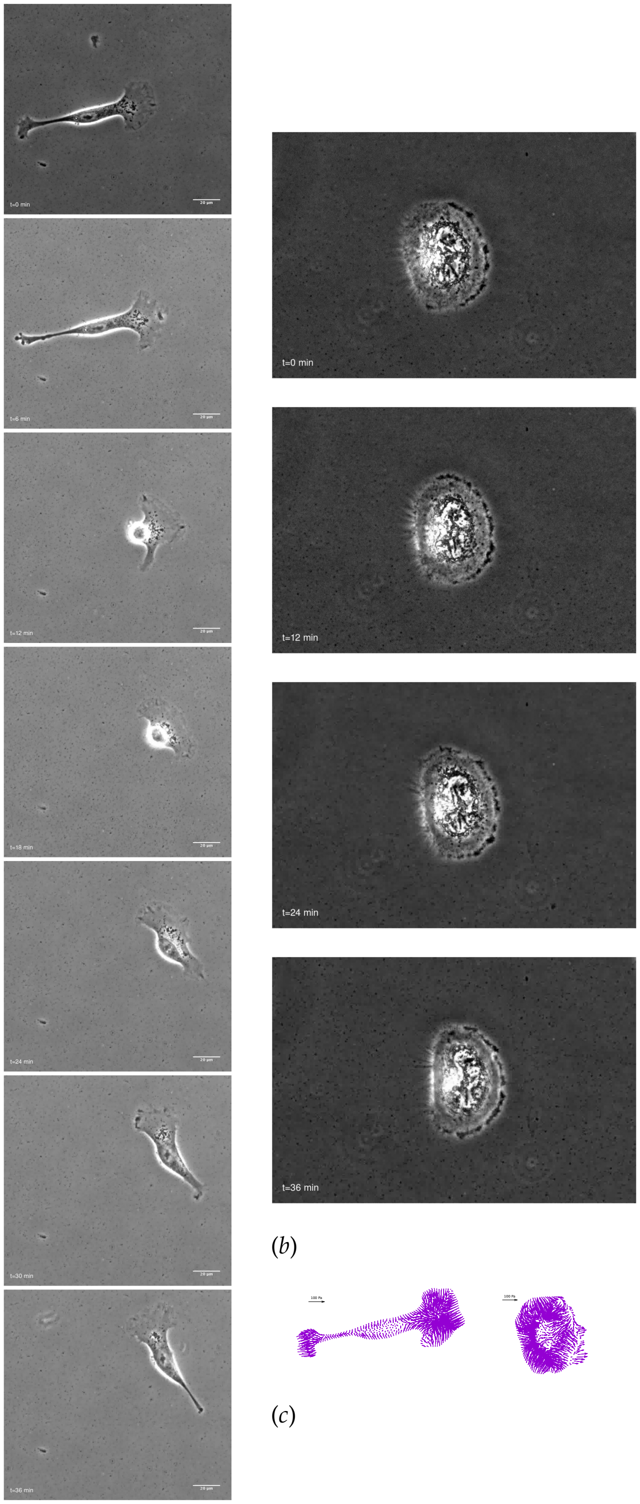

(*b*)

(*c*)

(*a*)

Figure 1: Migration of epithelial cancer cells on a 10 kPa substrate. (*a*) T24 cell line, (*b*) RT112 cell line. (*c*) Traction field recorded at selected instants for both cells.

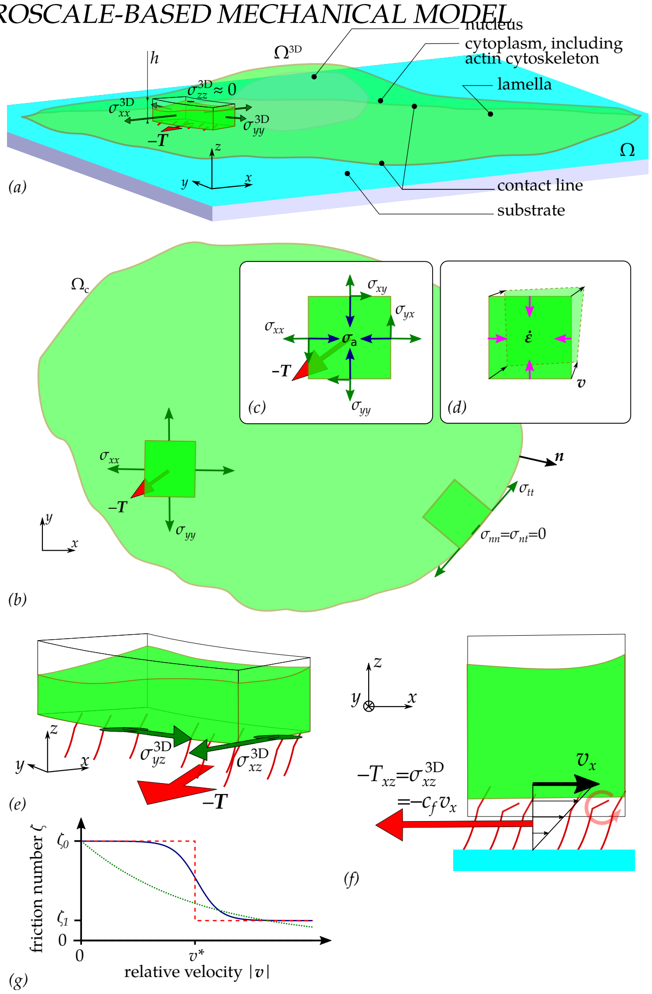

Figure 2: Mechanical balance and dynamics of the cell. (*a*) Three-dimensional mechanical balance. (*b*) Two-dimensional mechanical balance (top view). The two-dimensional stress tensor (components σ_{xx}, $\sigma_{xy} = \sigma_{yx}$, σ_{yy}) and the traction field $\boldsymbol{T}$ are defined over the cell domain Ω_c. The stress vanishes along $\partial\Omega_c$, $\boldsymbol{\sigma n} = \boldsymbol{0}$. (*c*) Stresses applied to a 2D element: the stress $\boldsymbol{\sigma}$ of the neighbouring actin elements is felt at the boundaries, the reaction force of the substrate for traction $\boldsymbol{T}$ is distributed over the area of the element, and $\boldsymbol{\sigma}_a$ is the pre-stress created by myosin contractility. Neglecting the fast elastic response for simplicity, the resultant of these stresses must be balanced by viscous stresses, equal to $\tau_\alpha G\dot{\boldsymbol{\varepsilon}}$. (*d*) Rate-of-strain $\dot{\boldsymbol{\varepsilon}}$ of a 2D element and associated velocity field $\boldsymbol{v}$. (*e*) The traction force field $\boldsymbol{T}$, assumed tangential, is equal and opposite to the shear components ($\sigma^{3D}_{\alpha z}$ of $\boldsymbol{\sigma}^{3D}$ at the contact surface. (*f*) The binding of transmembrane adhesion complexes (red symbols) to actin is highly dynamic, resulting in an effective viscous friction law for $\boldsymbol{T}$. (*g*) The dependence of the friction number $\zeta = D^2 c_f(|\boldsymbol{v}|)/(L_f^2 c_f^0)$ on the local actin speed $|\boldsymbol{v}|$ is modelled in different ways: dashed red line, constant by piece (for 1D analytical model), solid blue line, decreasing hyperbolic tangent (for comparison with [16] and numerical simulations), dotted red line, decreasing exponential (in good agreement with experimental measurements [30])

acting at boundaries where adhesion molecules are present is equal to the stress $\boldsymbol{T}$ that these exert on the environment at its boundaries.

As the actin flows, its density ρ will evolve. However, there is strong experimental evidence that the density of actin is tightly regulated by filament nucleators and various molecules favouring growth or shrinkage of actin filaments [32]. Denoting by $\bar{\rho}$ the target density field of this regulation, and assuming that it has a characteristic time τ_ρ, we can write describe this with an advection–reaction equation:

$$\frac{\partial \rho}{\partial t} + \boldsymbol{\nabla} \cdot (\rho \boldsymbol{v}^{3\mathrm{D}}) = \frac{1}{\tau_\rho}(\bar{\rho} - \rho)$$

where $\boldsymbol{v}^{3\mathrm{D}}$ is the velocity of actin. In what follows, we will assume $\tau_\rho \ll D/|\boldsymbol{v}^{3\mathrm{D}}|$, where D is the cell diameter, which leads to the solution of the above equation $\rho \simeq \bar{\rho}$, a uniform constant. This is supported by fluorescent speckle microscopy [33] and indeed, although there are visible local variations in the actin density on fluorescence images, the distribution of fluorescence intensity is well peaked and has a standard deviation of less than 50% of the peak intensity.

When adhering on a substrate of sufficiently large stiffness [34], cells spread until their projected surface $\Omega_\mathrm{c} = \left\{(x, y) \mid \exists\, z,\ (x, y, z) \in \Omega^{3\mathrm{D}}\right\}$ has a diameter D of the order 40 (RT112) to 100 μm (T24), and present a flat structure called the lamella [33] whose height is typically less than a few microns, and a dome-like structure referred to as the actin-cap, under which the nucleus is located, which has a height of 5 to 10 μm [35]. In the present work, we will consider that this aspect ratio is sufficiently small to justify a two-dimensional approach in which the cell is treated as a thin layer of thickness h subject to tangential surface tractions $\boldsymbol{T}$ and bulk forces $\boldsymbol{F}$ only, but it should be borne in mind that this is only a first approximation. In this context, we will consider also that the variations of h are small. This geometric setting constrains some components of the 3D stress tensor $\boldsymbol{\sigma}^{3\mathrm{D}}$: we have $\sigma^{3\mathrm{D}}_{zz} = 0$ and $\partial_z \sigma^{3\mathrm{D}}_{\alpha z} = -T_\alpha / h$ for $\alpha \in \{x, y\}$ [36], figure 2*e*, which allows to rewrite the problem in terms of a 2D stress tensor, with components $\sigma_{\alpha\beta} = h\sigma^{3\mathrm{D}}_{\alpha\beta}$, and write the 2D force balance as

$$\boldsymbol{\nabla} \cdot \boldsymbol{\sigma} = h\boldsymbol{F} - h\partial_z \boldsymbol{\sigma}^{3\mathrm{D}} = h\boldsymbol{F} + \boldsymbol{T}.$$

See figure 2*a,b* for a sketch of this mechanical balance. In practice, $\boldsymbol{F} = \boldsymbol{0}$ as bulk forces such as gravity are negligible and no external force is applied on the cell. At the cell edge $\partial\Omega_\mathrm{c}$ (which is noted experimentally to correspond to the contact line of the cell with the substrate, $\partial\Omega^{3\mathrm{D}} \cap \{z = 0\}$), there is no specific line force so the stress tensor $\boldsymbol{\sigma}$ along this boundary must vanish, figure 2*b*,

$$\boldsymbol{\sigma}\boldsymbol{n} = \boldsymbol{0} \quad \text{on } \partial\Omega_\mathrm{c}. \tag{1}$$

The stress tensor $\boldsymbol{\sigma}$ needs then to be related with the deformations by a constitutive law. Since most of the intracellular stress is borne by the actin meshwork, it is the deformation of actin which is relevant to study in a first approximation. We have derived and validated such a rheology for the actomyosin cortex in [21], by taking into account the dynamics of crosslinkers that bind to actin and the input of mechanical energy by the myosin motor molecules. The dynamics of crosslinkers is modelled by a single constant residence time, τ_α, which was found to be of the order of 10^3 s for two cell types (fibroblasts and myoblasts). The myosin molecular motors, which are among the crosslinks that bind and unbind, are in addition responsible for a supplementary term in the constitutive relation, which reads as a pre-stress $\sigma_{\mathrm{a}} = (\tau_\alpha/\tau_{\mathrm{myo}}) G \alpha_{\mathrm{myo}} (\ell\beta)^2$, where α_{myo} is the fraction of crosslinkers which are myosin filaments, and effectuate a power-stroke of step length ℓ at frequency $1/\tau_{\mathrm{myo}}$. G is the elastic modulus of the crosslinked actin network and β is inversely proportional to its Kuhn length. In [37], we have shown that the fluorescence intensity of labelled myosin molecules could provide a proxy for the local variations of α_{myo}, however here, in the absence of measurements for most of individual terms in σ_{a}, we will treat it globally as a constant, as was done successfully in [21]. For the sake of simplicity, we will also assume that the actin filaments are isotropically distributed in the plane parallel to the substrate, and define the pre-stress tensor $\boldsymbol{\sigma}_{\mathrm{a}} = \sigma_{\mathrm{a}} \boldsymbol{I}$. With these assumptions, the constitutive equation writes:

$$\tau_\alpha \overset{\triangledown}{\boldsymbol{\sigma}} + \boldsymbol{\sigma} - \tau_\alpha \kappa \operatorname{tr} \dot{\boldsymbol{\varepsilon}} - 2\tau_\alpha G \dot{\boldsymbol{\varepsilon}} = \boldsymbol{\sigma}_{\mathrm{a}}, \tag{2}$$

where $\dot{\boldsymbol{\varepsilon}}$ is the rate-of-strain tensor, $\overset{\triangledown}{\boldsymbol{\sigma}}$ the objective upper-convected time-derivative of the stress tensor $\boldsymbol{\sigma}$, and κ is Lamé's first coefficient. The group $\tau_\alpha G$ has the dimension of a viscosity and this terms corresponds to the energy dissipated in (slowly) deforming the actomyosin network [38] in an irreversible manner due to crosslinker unbinding [21]. This balance of stresses and the deformations linked with the viscous stresses are described in figure 2*c,d*. This rheology is in line with early models of actomyosin [39] and active gels models [40]. We do not supplement this contractile liquid behaviour with an elastic resistance term of the cell, contrarily to what is done in mechanosensing [41, 42] and migration models [17]. Other models have also considered the same rheology for cell migration, with an additional inertial term used for numerical stabilisation [4].

Finally, a rheological law must be proposed for the relationship between the traction forces $\boldsymbol{T}$ and the relative displacement between the substrate and the cell [3, 36]. Here again, the relevant structure to define a displacement within the cell is the actin meshwork, which is mechanically bound to adhesion molecules. In a first approximation, we assume that the substrate displacement rate is small compared to the velocity of the actin within the cell, $|\dot{\boldsymbol{u}}_s| \ll |\boldsymbol{v}|$. This hypothesis will need to be questioned in future work, as experiments show that substrate displacement rates are of the order of 10^{-3} µm/s, comparable with the speed of retrograde flow. With this simplifying hypothesis, the relative speed of actin with respect to the substrate is the velocity $\boldsymbol{v}$ of actin in the laboratory reference frame, and $\dot{\boldsymbol{\varepsilon}} = \frac{1}{2}(\boldsymbol{\nabla}\boldsymbol{v} + \boldsymbol{\nabla}\boldsymbol{v}^{\mathrm{T}})$. On the ground that adhesion complexes are very dynamic [11], we can expect a friction-like behaviour, figure 2*f*,

$$\boldsymbol{T} = c_f(|\boldsymbol{v}|)\boldsymbol{v}, \tag{3}$$

where c_f may depend on the velocity $|\boldsymbol{v}|$. This is assumed in many modelling approaches, including [28, 17] where c_f is taken constant, and in [43] where position-dependent and dissymmetric adhesion is implemented.

However, experiments show that although local traction force and actin velocity are positively correlated on the whole, above some critical velocity the traction forces drop by several folds [30, 16], indicating that c_f is not uniformly constant. The causes of the drop in c_f are only speculated, since locations with a lower c_f share three related characteristics: the actin flow speed is above a threshold v^* which seems to be a cell-type specificity ($v^* \simeq 0.2$ μm/s in fast-migrating keratocytes [16], $v^* \simeq 0.01$ μm/s in mammalian Ptk1 epithelial cells [30]), they are located more distally and adhesion complexes there are less mature [30]. In [16], they propose a differential equation that implements these different effects. Note that the precise role of the different terms in this model has not been experimentally tested so far, and [16] claim that a simple algebraic relation as exemplified in figure 2*g* captures the phenomenology. We choose to use the same algebraic relationship as they do, $c_f = c_f(|\boldsymbol{v}|)$, in order to test whether it is able to produce a fair quantitative prediction of traction stresses.

The modelling discussed so far describes only a (dynamic) mechanical equilibrium, giving a snapshot of the force balance and rate of strain of the actin network. It is not in the scope of the present paper to try to predict the subsequent dynamics of the cell, which would require to describe also processes such as actin polymerisation-based protrusion [2], or to provide some other more or less explicit dissymetrisation of the dynamics. Indeed, in order to obtain a persisting motility, models require a more or less explicit dissymetrisation either of the actin treadmilling [28, 44], of the myosin contractility σ_a [45, 16] or of the curvature of a contractile structure [15]. In one dimension, the need for such an effect can be proven [46]. Here, we show that the traction forces observed in cells are not dominated by this dissymetrical component, since an entirely symmetrical model allows us to give good predictions of the observations. Further refinement of the model and comparison with the experiments, and new experiments tracking explicitely myosin and adhesion molecules will be needed in the future to address this question.

Two length scales appear in the problem: one, the cell diameter D, is directly observable but depends on cell type and fluctuates during migration, the other is a friction length $\sqrt{\tau_\alpha G / c_f}$. The speed of retrograde flow v_t measured at the leading edge in [47] and calculated from the modelling of cell-scale experiments in [21] is convenient to scale the rate of deformation of the cytoskeleton: since v_t is of the order 10^{-3} to 10^{-2} μm/s, and the cell radius of the order of tens of microns, a characteristic time is $T = 10^3$ to 10^4 s. The other timescale in the problem is the relaxation time τ_α, in [21] we find $\tau_\alpha \simeq 10^3$ s: thus the viscoelastic term $\tau_\alpha \overset{\triangledown}{\boldsymbol{\sigma}}$ can be expected to be of a lower magnitude than $\boldsymbol{\sigma}$ in the consitutive equation (2), although it is not *a priori* negligible. If we choose to scale stresses with $\tau_\alpha v_\mathrm{t} G/D$, the nondimensional model is:

$$\zeta \tilde{\boldsymbol{v}} - \tilde{\boldsymbol{\nabla}} \cdot \tilde{\boldsymbol{\sigma}} = 0, \tag{4a}$$

$$\mathrm{De}\ \overset{\triangledown}{\tilde{\boldsymbol{\sigma}}} + \tilde{\boldsymbol{\sigma}} - \frac{\kappa}{G} \mathrm{tr}\, \tilde{\boldsymbol{\varepsilon}} - 2\tilde{\boldsymbol{\varepsilon}} = \tilde{\boldsymbol{\sigma}}_\mathrm{a}. \tag{4b}$$

where we introduce the friction nondimensional number $\zeta = D^2 c_f(|\boldsymbol{v}|)/(L_f^2 c_f^0)$, based on a friction length $L_f = \sqrt{\tau_\alpha G / c_f^0}$ for some reference friction coefficient c_f^0, and the Deborah number $\mathrm{De} = \tau_\alpha v_\mathrm{t}/D$.

4 Results

4.1 One-dimensional model predictions

In order to reach a good understanding of the mechanical balance that the model describes, we first study it in 1D. The cell is assumed to occupy a segment of the real axis, and since we do not introduce explicitly a dissymetry, our model will predict a solution which is symmetrical with respect to the midpoint of this segment. This simplistic setting thus corresponds to cells which are not migrating or polarised. The nondimensional equations for the permanent regime on the domain $(-1, 1)$ are:

$$-\zeta v + \partial_x \sigma = 0, \tag{5a}$$

$$\mathrm{De}(\partial_t \sigma + v \partial_x \sigma - 2\sigma \partial_x v) + \sigma = \partial_x v + \sigma_\mathrm{a}, \tag{5b}$$

$$\sigma = 0 \quad \text{at } x = \pm 1, \tag{5c}$$

where we have slighlty changed the nondimensionalisation, using $\kappa^{1\mathrm{D}} + 2G^{1\mathrm{D}}$ instead of G when scaling stresses. Note the nonlinear coupling term $2\mathrm{De}\, \sigma \partial_x v$, which arises from the upper-convected objective derivative of the stress tensor, in [36, 43] an analogue 1D model with the co-rotational derivative is proposed.

Analytical solutions can be obtained in the case $\mathrm{De} = 0$, and numerical approximations otherwise, the solution procedure is described in supplementary text **??**. An example of dynamical mechanical equilibrium is shown in figure 3*b*, for the case of a uniform friction number $\zeta = \zeta_0$ and a vanishing relaxation time $\mathrm{De} = 0$. A centripetal flow,

$$v(x) = -\frac{\sigma_\mathrm{a}}{\sqrt{\tau_\alpha G\, c_f}} \frac{\sinh(x\sqrt{\zeta})}{\cosh\sqrt{\zeta}},$$

corresponding to the retrograde flow, is observed [36]. It is maximal close to the cell edge, and its intensity is proportional to the myosin activity σ_a, consistent with experiments [33, 47]. The traction force density T pattern is by hypothesis directly proportional to the retrograde flow here, and thus centripetal and maximal close to cell edges too. The stress in the actomyosin vanishes at the cell

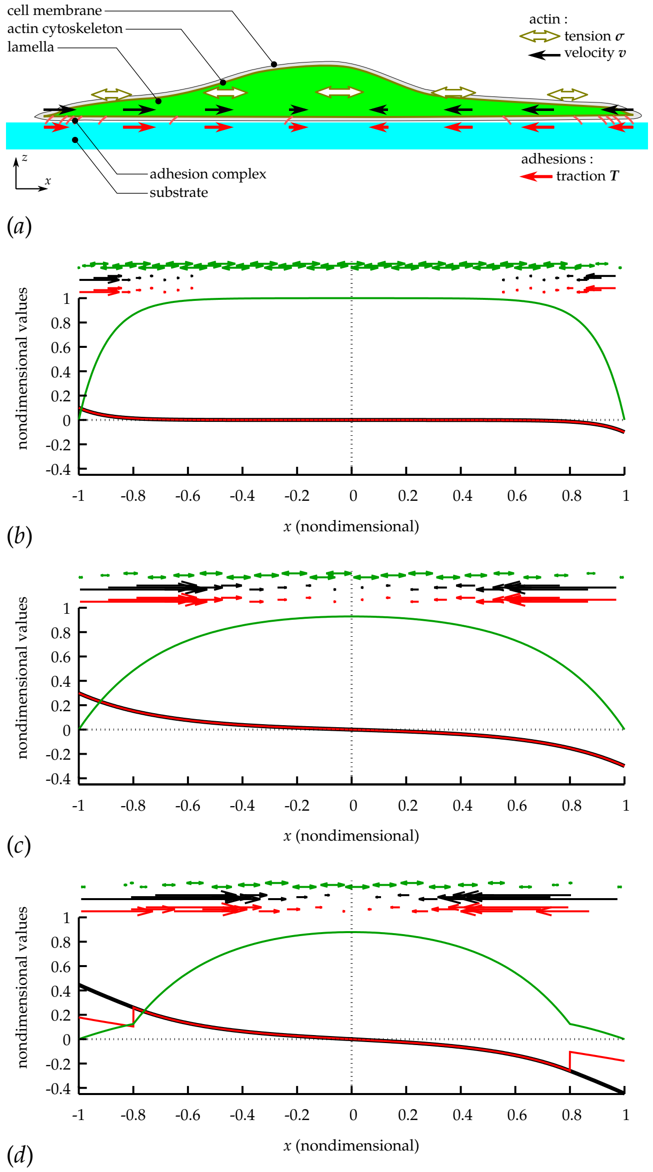

Figure 3: One-dimensional model and results (see full caption on page 11).

Figure 3: One-dimensional model and results (see figure on page 10). (*a*) Schematic of the relevant structures for cell mechanics and of the variables of interest. We define the stress tensor $\boldsymbol{\sigma}$ and the velocity $\boldsymbol{v}$ of the filamentous actin network at every point of the 1D domain corresponding to the cell. The cell interacts with its environment mostly through specific adhesion complexes, which link the intracellular actin network with the substrate, we name $\boldsymbol{T}$ the traction forces that actin exerts on the substrate via these adhesions. The relationship between stress tensor $\boldsymbol{\sigma}$ and velocity $\boldsymbol{v}$ is modelled by the rheological constitutive law (2), the relationship between the relative velocity of actin with respect to the substrate $\boldsymbol{v}$ and the traction force field $\boldsymbol{T}$ is given by the friction model (3). *(b)* Analytical result of system (5) with $\mathrm{De} = 0$, $\sigma_{\mathrm{a}} = 1$ and a uniform friction with friction length $L_f = 0.1D$. The stress tensor $\boldsymbol{\sigma}$ (reduced to its xx component), velocity $\boldsymbol{v}$ and traction field $\boldsymbol{T}$ are represented by their magnitude (respectively, green, black and red curves) and vector or tensor representation (green, black and red arrows or double-pointing arrows). The stress is mostly constant and positive in the cell lamella and body, corresponding to a tension, which is balanced by centripetal traction forces concentrated at the periphery. The tension gives rise to a deformation rate of the actin, resulting in the retrograde flow. *(c)* Same as (b) but with $L_f = 0.3D$. The weaker friction number leads to a wider peripheral zone of large tractions, but also to build up a lower tensile stress $\boldsymbol{\sigma}$, as the actin yields more and flows at higher velocity. *(d)* Same as (c) but with a nonuniform friction number, equation (6), $\zeta_1/\zeta_0 = 0.16$, and $v^* = 0.26$.

edge, which corresponds to our imposed boundary condition, and is maximal at the cell center in proportion with myosin activity σ_a:

$$\sigma(x) = \sigma_\text{a}\left(1 - \frac{\cosh\left(x\sqrt{\zeta}\right)}{\cosh\sqrt{\zeta}}\right)$$

It is thus myosin activity that puts the actin network under tension, a tension which is balanced at the cell edges by friction via the friction number ζ. If ζ is large, the tension is constant in most of the domain and balanced by traction forces in a narrow zone close to the edge, figure 3*c*.

In the case when $\text{De} = 0.1$, which corresponds to our estimates for experimental cases, the solution differs little from the $\text{De} = 0$ solution, figure **??**. For $\text{De} \geq 1$, a quantitative deviation can be appreciated, supplementary figure **??**, but there is no strong qualitative difference. We will thus focus on the case $\text{De} = 0$ from this point, as this allows analytical 1D calculations and less involved numerical simulations in 2D (although the visco-elastic case $\text{De} > 0$ can be treated, see e.g. [48] using the approach in [49]).

We then turn to the case of a nonlinear friction number $\zeta = \zeta(|\boldsymbol{v}|)$, in order to allow analytical resolution we take a piecewise constant function, figure 2*g*:

$$\zeta(\boldsymbol{x}) = \begin{cases} \zeta_0 & \text{if } |\boldsymbol{v}(\boldsymbol{x})| < v^*, \\ \zeta_1 & \text{else,} \end{cases} \tag{6}$$

with $\zeta_1 < \zeta_0$ consistently with observations [30, 16]. In figure 3*d*, we see that this results in a more uniform the retrograde flow close to the cell edge, which is due to the fact that there is less of a gradient of tension there, due to a lower local friction. Because of the low friction number locally, traction is low close to the cell edge, which is the phenomenology that we wanted to reproduce.

Numerically, we can solve with $\zeta = \zeta_0 \exp(-|\boldsymbol{v}|/v^*)$, figure 2*g*, which is closer to the experimental observations [30], this gives a smoother behaviour but no essential qualitative difference.

4.2 Prediction of the traction field of a motile cell

Turning now to a two-dimensional approach, we ask whether for a given cell shape, the above model can predict the traction pattern that we measure by traction force microscopy, as in figure 1. Starting from the data of Ω_c for a typical experimental result, we calculate using a finite element approach (see section 6.3) the traction field for a linear friction law (c_f independent of $\boldsymbol{v}$) and a choice of the two parameters: friction number ζ_0 and myosin contractility σ_a. As in 1D, the magnitude of the stress, retrograde flow and traction forces are in direct proportion to σ_a (see supplementary text **??**), while changes in ζ_0 will modify the pattern of retrograde flow and traction forces. In consequence, we can find explicitly an optimal value for σ_a for a given value of ζ_0, and optimize for this parameter in order to get the best fitting approximation of the experimental traction field, figure 4*a*. The relative error on the traction vectors is $\left\|\boldsymbol{T}_h - \boldsymbol{T}_\text{exp}\right\| / \left\|\boldsymbol{T}_\text{exp}\right\| = 0.73$, that is, the error vectors $\boldsymbol{T}_h - \boldsymbol{T}_\text{exp}$

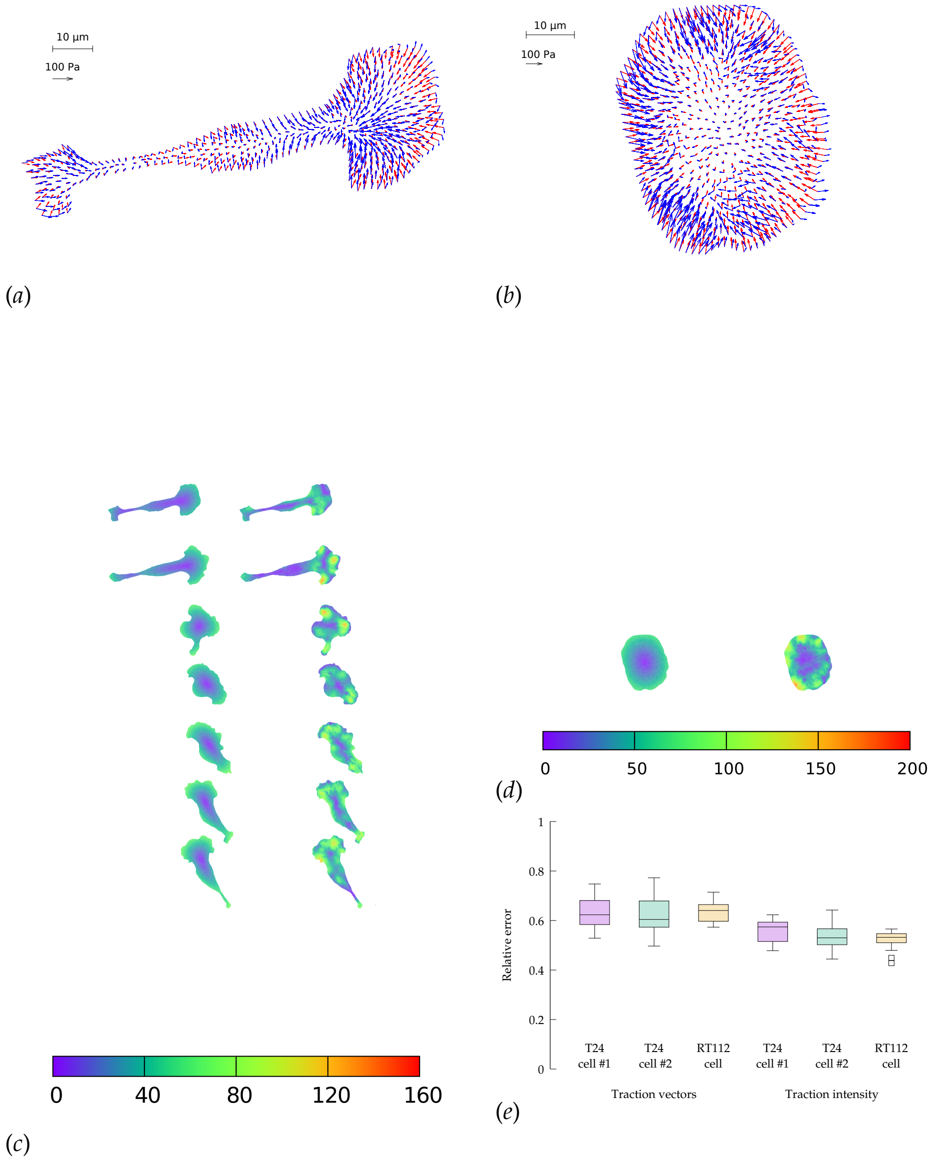

(*a*) (*b*) (*c*) (*d*) (*e*)

Figure 4: Two-dimensional linear model predictions compared to experimental results (see full caption on page 14).

Figure 4: Two-dimensional linear model predictions compared to experimental results (see figure on page 13). Throughout this figure, the friction number ζ is a uniform constant equal to ζ_0^*. The only two free parameters of the model are adjusted to $\zeta_0^* = 19.4$ and $\sigma_\mathrm{a}^* = 27.7$ (both nondimensional) so as to match best experimental traction field $\boldsymbol{T}_\mathrm{exp}$ in panel (a), they are used to predict traction fields for observed cell shapes Ω_c^i in panels (b)–(e). (*a*) Comparison of traction field predicted by the model (red arrows) and calculated from experimental observations (blue arrows) at the initial instant $t = 0$ of a migration experiment of a T24 cell. In the uropod (right), a good agreement is found with an alignment mismatch ranging from close to 0 up to nearly 90 degrees in a small subregion. In the slender part linking the uropod with the cell body, intensity of traction is low in predictions and experiment. Around the cell body (thicker part where the nucleus is located), the magnitude of traction is rather well predicted, and the alignment mismatch ranges from 0 to 45 degrees. The model predicts the observed tractions oriented from nucleus area towards the lamella at the cell front with a very good alignment and magnitude. Finally, in the lamella region (left), the global centripetal traction field is predicted, although the location of the maximal traction is not predicted: indeed, close to the leading edge, we note experimentally low tractions which cannot be reproduced by the linear model, and which may be due to unmature or rupturing adhesions. (*b*) Comparison of traction field predicted by the model (red arrows) and calculated from experimental observations (blue arrows) at the initial instant of a migration experiment of an RT112 cell. No parameter adjustment. The RT112 morphology is much simpler, and the model predicts a centripetal traction field which globally agrees with observations. The same shortcomings of the model as for the lamella region in T24 cells, panel (*a*), are noted. (*c*) Comparison of the field of traction intensity across a full migration cycle as predicted by the model (left) and calculated from experimental observations (right) for the T24 cell in panel (a). Magnitudes are given in Pascals. From top to bottom, a subsample of the experimentally recorded steps is presented, every 6 minutes ($t = 0$, 6, 12, 18, 24, 30, 36 min). No parameter adjustment was done for $t > 0$. Although the maximum traction observed experimentally is not always right at the leading edge, the global pattern and size of high-traction regions are predicted by the model throughout the migration cycle, across variations in cell area, aspect ratio and orientation. (*d*) Same for the RT112 cell in panel (b) at $t = 0$. See supplementary figure **??** for $t > 0$. Magnitudes are given in Pascals, no parameter adjustment. (*e*) Relative error of the predicted tractions compared to experiments for the $n = 21$ instants at which a frame was recorded in experiments. Relative error on traction vectors $\left\|\boldsymbol{T}_h - \boldsymbol{T}_\mathrm{exp}\right\| / \left\|\boldsymbol{T}_\mathrm{exp}\right\|$, and on intensity of traction $\left\||\boldsymbol{T}_h| - |\boldsymbol{T}_\mathrm{exp}|\right\| / \left\||\boldsymbol{T}_\mathrm{exp}|\right\|$ is presented for the three experiments on cell types T24 and RT112. No parameter adjustment was done for individual experiments and instants, ζ_0^* and σ_a^* are used throughout the $n = 66$ frames.

have a magnitude 0.73 times the experimental vectors $\boldsymbol{T}_{\text{exp}}$ in L^2 norm. This can be considered a fair result for a two-parameter fit of a vector field with rich features. Indeed, the experimental traction field at this instant indicates that there is probably no mature adhesion under the protrusion visible on the left hand side, since the traction field decreases dramatically there. This feature cannot described by this first model where the friction number is taken to be a homogeneous constant, thus limiting the possibility to approximate the experimental observations. The relative error on the intensity of traction is $\left\| |\boldsymbol{T}_h| - |\boldsymbol{T}_{\text{exp}}| \right\| / \left\| \boldsymbol{T}_{\text{exp}} \right\| = 0.59$, thus the error is shared between a mismatch between experimental and predicted magnitude of traction field, and some misalignment of the experimental and predicted traction vectors. The optimal parameters are found to be $\zeta_0^* \simeq 20$, which implies a friction length of the order of 10 µm, and $\sigma_{\text{a}}^* \simeq 30$. Using the numerical value of parameters τ_α and v_{t} that we have obtained in [21] for two other cell types, this would imply that the myosin pre-stress σ_{a} is about three times the zero-shear elastic modulus G of the actomyosin meshwork, in [21] the same ratio was found to be 4.3.

During the experiments, cell position and shape Ω_{c}^i and traction forces $\boldsymbol{T}_{\text{exp}}^i$ were acquired at several instants t^i two minutes apart. We now ask whether our model and the parameters σ_{a}^* and ζ_0^* can, for these different cell shapes Ω_{c}^i, predict the traction forces $\boldsymbol{T}_{\text{exp}}^i$ without further parameter adjustment. We find that for the 21 frames of the experimental results, the relative error on traction vectors ranges from 0.53 to a maximum of 0.75, with a median of 0.60, which indicates that the parameters that where optimal for one instant give as good results for other frames, figure 4*c*,*e*, even though the aspect ratio of the cell changes by a factor two depending on the stage of the migration process. The relative error on traction intensities ranges from 0.48 to 0.61, with a median of 0.57.

Thus the parameters describing the mechanical behaviour of a migrating T24 cell are approximately conserved over more than half an hour during crawling. We then tested whether these parameters could also predict a good approximation of the traction stresses exerted by another cell of the same type in the same conditions. The comparison of the predictions of the model, using the same values ζ_0^* and σ_{a}^* as for the first T24 cell, are shown in supplementary figure **??**, the error of the predicted traction field varies in the same range as for the first cell, figure 4*e*.

Next we considered the other cell type that was studied experimentally, RT112 cells. These cells spread to a much lower area on the substrate and maintain a rounded shape which evolves little in the course of migration. Although these characteristics are reminiscent of amoeboid migration, RT112 crawl at smaller speed and exert larger tractions than T24 [27]. All these characteristics make RT112 cells very different from T24, and we asked whether this is due to a different mechanical balance altogether, or different quantitative importance of several effects. However, when applying the same mechanical model as above with the parameters ζ_0^* and σ_{a}^*, a fair approximation of the traction

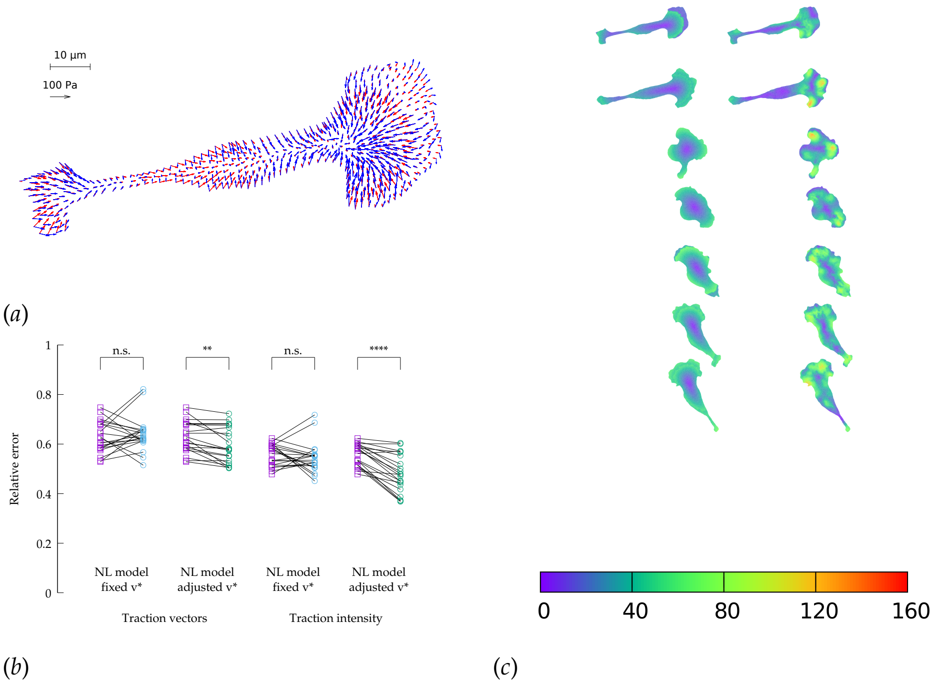

Figure 5: Two-dimensional nonlinear model predictions compared to experimental results (see full caption on page 17).

field obtained experimentally is recovered, figure 4*b*,*d*. This is equally true for the all 20 frames of this RT112 experiment, supplementary figure **??**, the median of the relative error on traction vectors is 0.41 and its range from 0.33 to 0.51, and traction intensities have a median error of 0.36 and a range from 0.22 to 0.42, figure 4*e*.

For both RT112 and T24 cell types, experimental results show that the traction field maxima are generally not located quite at the cell edge, but somewhat proximal from it. As seen in the 1D calculations, figure 3*d*, this is compatible with the model provided that there is a switch from a large friction number ζ_0 to a lower one ζ_1 above some relative velocity v^*. As seen on figure 5*a*, for an appropriate choice of these parameters, the model prediction is improved. The median error on traction vectors drops from 0.73 to 0.61 and the one on the traction intensity from 0.59 to 0.48, the better agreement is in a large part due

Figure 5: Two-dimensional nonlinear model predictions compared to experimental results. (see figure on page 16). Two of the free parameters of the model are kept equal to $\zeta_0^* = 19.4$ and $\sigma_a^* = 27.7$ (both nondimensional) as in figure 4. (*a*) Comparison of traction field predicted by the model (red arrows) and calculated from experimental observations (blue arrows) at the initial instant $t = 0$ of a migration experiment of a T24 cell. To the difference of figure 4*a*, a nonconstant friction number ζ is used (see figure 2*g*) and the additional parameters v^* and ζ_1 are adjusted so as to fit best the experimental data. Compared to figure 4*a*, the agreement in the large protrusion behind the cell leading edge (right) is better both in term of the local magnitude of traction field and in terms of the alignment in areas where the magnitude is large. The agreement is also better in one of the sides of the uropod (top left). (*b*) Paired test of the change in relative error for the nonlinear model with fixed v^* and with v^* adjusted at each frame. The test is relative to the linear case, results shown in figure 4*e*. The 'nonlinear (NL) model with fixed v^*' makes use of the nonconstant friction number ζ (figure 2*g*) whose extra parameters are adjusted on the first frame of the experiment only. The 'nonlinear model with adjusted v^*' corresponds to the same model, but extra parameters are adjusted on each frame of the experiment. There is no significant change in the case of fixed v^* ($p = 0.53$ and $p = 0.38$ for the two error measures, respectively), but the error significantly decreases at each frame when v^* is adjusted ($p = 0.010$ and $p = 1.4 \cdot 10^{-6}$, respectively). Significance tests were performed with a paired *t*-test with 20 degrees of freedom. (*c*) Comparison of the field of traction intensity across a full migration cycle as predicted by the nonlinear model (left) and calculated from experimental observations (right) for the T24 cell in panel (a). Magnitudes are given in Pascals. From top to bottom, a subsample of the experimentally recorded steps is presented, every 6 minutes ($t = 0, 6, 12, 18, 24, 30, 36$ min). Parameter adjustment was performed for v^* and ζ_1 only for $t > 0$.

to a better match in magnitude of the traction in the protrusion at the cell front, but also in a better match of the directionality of tractions in this area.

Next we asked whether this choice of parameters is robust in the same sense as the choice of ζ_0^* and σ_a^* allowed the linear model to be predictive of the tractions at later migration stages and for other cells. We find that if v^* and ζ_1 are assumed to remain constant across the different stages of migration, the nonlinear model does not significantly improve the match between predictions and experiments. However, if v^* is adjusted for each frame, we obtain a significant decrease of the error, figure 5*b*. In figure 5*c*, it is seen that the characteristic pattern of traction increase toward distal followed by an abrupt drop near the foremost areas of protrusions is recovered by this adhesion model.

5 Discussion

Cell migration is known to rely on a complex machinery subject to a large number of regulatory pathways [2]. Here however we show that cells which are migrating in a smooth way without shape changes (RT112) and cells which exhibit a multi-stage cycle of protrusion and retraction (T24) have a similar mechanical behaviour, whose baseline can be predicted with a simple model of actomyosin contraction and of adhesion. In particular, there is no obvious adjustment of the global mechanical balance corresponding to specific steps of mesenchymal migration, since all can be approximated with the same model parameters, which describe the myosin activity (pre-stress) and the effective friction due to the dynamics of adhesions.

This tends to imply that in a significant measure, the dynamics of actomyosin and of adhesions are not orchestrated at the time scale of the migration steps, but left to their self-organised assembly and disassembly pace. As shown in [21], this is not in contradiction with the 'sensing' properties of actomyosin, since the collective dynamics of actin and myosin give an emergent material which is intrinsically sensitive to the mechanical behaviour of the environment, even in the absence of a regulatory signal. This reliance of the mechanics of motility on self-organised processes is in agreement with the robustness of this behaviour—indeed even lamellar fragments of cells lacking nuclei, microtubules and most organelles can exhibit motility [13]. This is not to say that regulation via biochemical pathways would not be crucial to the migration process, but rather that they need to act only in order to tune an otherwise self-maintained system, just as adjusting the throttle control of an engine.

Beyond the fact that the global mechanical balance is well approximated, the traction fields observed contain many further details that cannot be captured by the linear model. The most prominent of these are the decreased traction forces at the leading edges, which are noted at most stages of mesenchymal migration in both T24 cells figure 5*c*, supplementary figure **??** and RT112 cells supplementary figure **??**, and had been noted in the literature before [30, 16]. We find that these features can be reproduced by a nonlinear model which includes a velocity-dependent friction coefficient. In [30], they conclude from experimental data on local traction and actin velocity that the ageing and maturation of adhesion complexes are not correlated with their strength, and that the switch is based on a critical velocity v^*. Here we find however that the critical velocity v^*, contrarily to the myosin contractile pre-stress σ_{a}, varies at the scale of a few minutes during cell crawling. This suggests that v^* may be the target of a biochemical regulation that would be coupled with the migration steps.

6 Appendix: Methods

6.1 Cell crawling assays and image analysis

The detailed protocol is described in [27]. Briefly, 10 kPa-polyacrylamide gels were prepared with 0.2-μm fluorescent beads and coated with fibronection. Epithelial bladder cancer cell lines T24 and RT112 were seeded on the gel and left overnight to spread. Images were acquired with a time interval of 120 seconds for 2 hours. The cell shape Ω_{c} was acquired either by transmission microscopy or by fluorescence reflection microscopy of actin-GFP transfected cells. Within a domain Ω (the field of view), the position $\boldsymbol{x}_j^i$ of bead j in frame i is obtained with 'ParticleTracker' [50] in ImageJ software, the relaxed (also called initial) bead position $\boldsymbol{x}_j^0$ is actually acquired at the end of the experiment by detaching cells using distilled water, allowing to construct the set of displacements $\boldsymbol{u}^i_{\mathrm{exp}}(\boldsymbol{x}) = \sum_j (\boldsymbol{x}_j^i - \boldsymbol{x}_j^0)\delta_{\boldsymbol{x}_j^i}(\boldsymbol{x})$ (see [51] for details). Ω is chosen so that $|\boldsymbol{u}_{\mathrm{exp}}|$ is vanishingly small close to $\partial\Omega$. We note that generally speaking, $|\boldsymbol{u}^i_{\mathrm{exp}}(\boldsymbol{x}_j)| \lesssim 1$ μm while the diameter of Ω_{c} is of the order of 50 μm.

6.2 Traction force inverse problem resolution

Details can be found in [27, 52, 53]. The mechanical characterization of the gel is approximated as isotropic and elastic and the displacements are observed to be small enough so that linear elasticity applies. We assume that the gel can be approximated by a half-space $\{z \leq 0\}$, the gel depth of 70 μmis sufficient to guarantee this for RT112 cells which have a diameter of 50 μm[54], but can introduce an error on some of the frames of the T24 cell migration, since it can transiently reach a length of the order of 100 μm. Following [25], a reduced 2D problem is obtained by averaging in z over an effective thickness w (typicall 1.5 μm) and the adjoint problem is written on $\Omega \subset \{z = 0\}$ in terms of an auxiliary unknown $\boldsymbol{p}$:

$$-\mu\Delta\boldsymbol{u}_{\mathrm{s}} - (\lambda + mu)\boldsymbol{\nabla}(\boldsymbol{\nabla}\cdot\boldsymbol{u}_{\mathrm{s}}) = -\frac{\chi_{\mathrm{c}}}{\varepsilon}(\boldsymbol{p} - \bar{\boldsymbol{p}}) \qquad \text{in } \Omega, \quad \boldsymbol{u}_{\mathrm{s}} = \boldsymbol{0} \text{ on } \partial\Omega \tag{7a}$$

$$-\mu\Delta\boldsymbol{p} - (\lambda + mu)\boldsymbol{\nabla}(\boldsymbol{\nabla}\cdot\boldsymbol{p}) = \chi_{\mathrm{exp}}(\boldsymbol{u}_{\mathrm{s}} - \boldsymbol{u}_{\mathrm{exp}}) \quad \text{in } \Omega, \quad \boldsymbol{p} = \boldsymbol{0} \text{ on } \partial\Omega \tag{7b}$$

where χ_{c} is the indicator function of Ω_{c}, $\chi_{\mathrm{exp}} = \sum_j \delta_{\boldsymbol{x}_j^0}(\boldsymbol{x})$, $\bar{p} = \int_{\Omega_{\mathrm{c}}} \boldsymbol{p}\, \mathrm{d}\boldsymbol{x}$ is the resultant of $\boldsymbol{p}$ over Ω_{c} and the reduced 2D Lamé coefficients are $\mu = \frac{wE}{2(1+\nu)}$ and

$\lambda = \frac{wE\nu}{1-\nu^2}$. Problem (7) is solved for all frames i using a finite element method on a triangulation $\mathcal{T}_h^i = \mathcal{T}_{\mathrm{c},h}^i \cup \mathcal{T}_{\mathrm{o},h}^i$ of Ω, where $(\boldsymbol{x}_j^i)_j$ are among the nodes and $\mathcal{T}_{\mathrm{c},h}^i$ is a triangulation of a polygonal approximation $\Omega_{\mathrm{c},h}$ of order h^2 of Ω_c. The calculated traction field is $\boldsymbol{T}_\mathrm{exp} = -\frac{\chi_\mathrm{c}}{\varepsilon}(\boldsymbol{p} - \bar{\boldsymbol{p}})$, which vanishes in $\Omega \setminus \Omega_\mathrm{c}$ and has zero resultant. For the same reason as the resultant is zero, the torque of the traction field also has to be zero. However, we do not enforce this currently in the method and the fact that the torque is small is only checked *a posteriori* on the calculated traction field.

6.3 Finite-element simulations and parameter fitting

In section 3, we derive a tensorial visco-elastic model allowing to predict cell traction field $\boldsymbol{T}_h$ from the knowledge of cell shape Ω_c and some scalar parameters, namely σ_a, ζ_0, and in the nonlinear case ζ_1 and v^*. The algorithm for the resolution of the full visco-elastic problem is given in [48]. Here we show in one dimension that within the range of experimentally-relevant parameters, visco-elastic effects do not affect strongly the results. Thus simulations are shown only for the reduced viscous limit.

Briefly, we define a finite element space V_h of piecewise quadratic functions based on the triangulation $\widetilde{\mathcal{T}}_{\mathrm{c},h}^i$ of $\widetilde{\Omega}_\mathrm{c}$ at frame i, where $\widetilde{\Omega}_\mathrm{c}$ is the cell domain Ω_c observed experimentally but with distances normalized by $D = 50$ μm. Using the finite element software Rheolef, we solve the variational problem, supplementary equation (**??**), in V_h for a given choice of $\sigma_\mathrm{a} = \sigma_\mathrm{a}^1$ and a uniform $\zeta = \zeta_0$ for a solution $\boldsymbol{v}_{h,0}^1$. In the case of nonlinear friction, ζ depends on $\boldsymbol{v}$, a fixed-point algorithm is used to construct a sequence of solutions $\boldsymbol{v}_{h,k}^1$ using the friction field $\zeta(\boldsymbol{x}) = \zeta(|\boldsymbol{v}_{h,k-1}^1|(\boldsymbol{x}))$, until convergence.

Next, the parameters can be optimized in order to best fit the experimental observations $\boldsymbol{T}_\mathrm{exp}$. Note that best-fit is performed on one cell at the initial frame only throughout the paper to acquire parameters σ_a and ζ_0, no fitting is done for the other frames and the other cells. We normalize $\boldsymbol{T}_\mathrm{exp}$ by a typical value 100 Pa, and aim to minimize $\left\|\boldsymbol{T}_h - \widetilde{\boldsymbol{T}}_\mathrm{exp}\right\|$ by adjusting ζ_0 and σ_a. Thanks to the linearity of operators and the scale-invariance of our choices for the function ζ (see supplementary text **??**), minimisation for a given ζ_0 with respect to σ_a can be done explicitly, and the minimisation writes:

$$\sigma_\mathrm{a}^* = \frac{\int_{\widetilde{\Omega}_\mathrm{c}} \widetilde{\boldsymbol{T}}_\mathrm{exp} \cdot \boldsymbol{T}_h^1 \,\mathrm{d}\boldsymbol{x}}{\left\|\boldsymbol{T}_h^1(\zeta_0)\right\|}\sigma_\mathrm{a}^1, \qquad \zeta_0^* = \arg\min_{\zeta_0} \left\| \left(\widetilde{\boldsymbol{T}}_\mathrm{exp} - \frac{\sigma_\mathrm{a}^*}{\sigma_\mathrm{a}^1} \boldsymbol{T}_h^1(\zeta_0) \right) \right\|.$$

In the rest of the article, we denote $\widetilde{\Omega}_\mathrm{c}$ and $\widetilde{\boldsymbol{T}}_\mathrm{exp}$ simply by Ω_c and $\boldsymbol{T}_\mathrm{exp}$.

Acknowledgements

J.E. thanks the Isaac Newton Institute for Mathematical Sciences for its hospitality during the programme *Coupling Geometric PDEs with Physics for Cell*

Morphology, Motility and Pattern Formation supported by EPSRC Grant Number EP/K032208/1. All authors thank Région Rhône-Alpes (CIBLE), ANR-12-BS09-0020-01 ”Transmig” and Tec21 (ANR-11-LABX-0030), and all except A.D. are member of GDR 3570 *MécaBio* and GDR 3070 *CellTiss* of CNRS.

References

[1] P. Friedl and K. Wolf. Tumour-cell invasion and migration: Diversity and escape mechanisms. *Nature Rev. Cancer*, 3:362–374, 2003.

[2] D. A. Lauffenburger and A. F. Horwitz. Cell migration: a physically integrated molecular process. *Cell*, 84:359–369, 1996.

[3] W. Alt and M. Dembo. Cytoplasm dynamics and cell motion: two-phase flow models. *Math. Biosci.*, 156:207–228, 1999.

[4] B. Rubinstein, M. F. Fournier, K. Jacobson, A. Verkhovsky, and A. Mogilner. Actin-myosin viscoelastic flow in the keratocyte lamellipod. *Biophys. J.*, 97:1853–1863, 2009.

[5] S. Banerjee and M. C. Marchetti. Substrate rigidity deforms and polarizes active gels. *Europhys. Lett.*, 96:28003, 2011.

[6] J. Lee, A. Ishihara, J. A. Theriot, and K. Jacobson. Principles of locomotion for simple-shaped cells. *Nature*, 362:167–171, 1993.

[7] T. D. Pollard and G. G. Borisy. Cellular motility driven by assembly and disassembly of actin filaments. *Cell*, 112:453–465, 2003.

[8] D. Bray and J. G. White. Cortical flow in animal cells. *Science Mag.*, 239:883–888, 1988.

[9] J. A. Theriot and T. J. Mitchison. Comparison of actin and cell surface dynamics in motile fibroblasts. *J. Cell Biol.*, 119:367–77, 1992.

[10] J. V. Small and G. P. Resch. The comings and goings of actin: coupling protrusion and retraction in cell motility. *Curr. Opinion Cell Biol.*, 17:517–523, 2005.

[11] J. T. Parsons, A. R. Horwitz, and M. A. Schwartz. Cell adhesion: integrating cytoskeletal dynamics and cellular tension. *Nat. Rev. Mol. Cell Biol.*, 11:633–643, 2011.

[12] T. P. Stossel. On the crawling of animal cells. *Science*, 260:1086–1094, 1993.

[13] A. B. Verkhovsky, T. M. Svitkina, and G. G. Borisy. Self-polarization and directional motility of cytoplasm. *Curr. Biol.*, 9:11–20, 1999.

[14] E. L. Barnhart, K. C. Lee, K. Keren, A. Mogilner, and J. A. Theriot. An adhesion-dependent switch between mechanisms that determine motile cell shape. *PLoS Biol.*, 9:e1001059, 2011.

[15] C. Blanch-Mercader and J. Casademunt. Spontaneous motility of actin lamellar fragments. *Phys. Rev. Lett.*, 110:078102, 2013.

[16] E. Barnhart, K.-C Leeb, G. M. Allen, J. A. Theriot, and A. Mogilner. Balance between cell–substrate adhesion and myosin contraction determines the frequency of motility initiation in fish keratocytes. *Proc. Natl. Acad. Sci. USA*, 112:5045–5050, 2015.

[17] P. Recho, T. Putelat, and L. Truskinovsky. Mechanics of motility initiation and motility arrest in crawling cells. *J. Mech. Phys. Solids*, 84:469–505, 2015.

[18] B. Alberts, Alexander Johnson, J. Lewis, M. Raff, K. Roberts, and P. Walter. *Molecular Biology of the Cell*. Garland Science, 4th edition, 2002.

[19] P. W. Oakes, S. Banerjee, M. C. Marchetti, and M. L. Gardel. Geometry regulates traction stresses in adherent cells. *Biophys. J.*, 107:825–838, 2014.

[20] C. Labouesse, A. B. Verkhovsky, J.-J. Meister, C. Gabella, and B. Vianay. Cell shape dynamics reveal balance of elasticity and contractility in peripheral arcs. *Biophys. J.*, 108:2437–2447, 2015.

[21] J. Étienne, J. Fouchard, D. Mitrossilis, N. Bufi, P. Durand-Smet, and A. Asnacios. Cells as liquid motors: Mechanosensitivity emerges from collective dynamics of actomyosin cortex. *Proc. Natl. Acad. Sci. USA*, 112:2740–2745, 2015.

[22] A. K. Harris, P. Wild, and D. Stopak. Silicone rubber substrata: a new wrinkle in the study of cell locomotion. *Science*, 208:177–179, 1980.

[23] M. Dembo and Y.-L. Wang. Stresses at the cell-to-substrate interface during locomotion of fibroblasts. *Biophys. J.*, 76:2307–2316, 1999.

[24] J.P. Butler, I.M. Toli-Norrelykke, B. Fabry, and J.J. Fredberg. Traction fields, moments, and strain energy that cells exert on their surroundings. *Am. J. Physiol. Cell Physiol.*, 282:C595–C605, 2002.

[25] D. Ambrosi. Cellular traction as an inverse problem. *SIAM J. Appl. Math.*, 66:2049–2060, 2006.

[26] U. S. Schwarz and M. L. Gardel. United we stand – integrating the actin cytoskeleton and cell–matrix adhesions in cellular mechanotransduction. *J. Cell Sci.*, 125:3051, 2012.

[27] V. Peschetola, V. M. Laurent, A. Duperray, R. Michel, D. Ambrosi, L. Preziosi, and C. Verdier. Time-dependent traction force microscopy for cancer cells as a measure of invasiveness. *Cytoskeleton*, 70:201–214, 2013.

[28] K. Kruse, J.-F. Joanny, F. Jülicher, and J. Prost. Contractility and retrograde flow in lamellipodium motion. *Phys. Biol.*, 3:130–137, 2006.

[29] B. L. Bangasser and D. J. Odde. Master equation-based analysis of a motor-clutch model for cell traction force. *Cell. Mol. Bioengng*, 6:449–459, 2013.

[30] M. L. Gardel, B. Sabass, L. Ji, G. Danuser, U. S. Schwarz, and C. M. Waterman. Traction stress in focal adhesions correlates biphasically with actin retrograde flow speed. *J. Cell Biol.*, 183:999, 2008.

[31] E. Moeendarbary, L. Valon, M. Fritzsche, A. R. Harris, D. A. Moulding, A. J. Thrasher, E. Stride, L. Mahadevan, and G. T. Charras. The cytoplasm of living cells behaves as a poroelastic material. *Nature Mater.*, 12:253–261, 2013.

[32] C. Le Clainche and M.-F. Carlier. Regulation of actin assembly associated with protrusion and adhesion in cell migration. *Physiol. Rev.*, 88:489–513, 2008.

[33] A. Ponti, M. Machacek, S. L. Gupton, C. M. Waterman-Storer, and G. Danuser. Two distinct actin networks drive the protrusion of migrating cells. *Science*, 305:1782–1786, 2004.

[34] T. Yeung, P. C. Georges, L. A. Flanagan, B. Marg, M. Ortiz, M. Funaki, N. Zahir, W. Ming, V. Weaver, and P. A. Janmey. Effects of substrate stiffness on cell morphology, cytoskeletal structure, and adhesion. *Cell Motil. Cytoskeleton*, 60:24–34, 2005.

[35] D. F. Burnette, Lin Shao, C. Ott, A. M. Pasapera, R. S. Fischer, M. A. Baird, C. Der Loughian, H. Delanoe-Ayari, M. J. Paszek, M. W. Davidson, E. Betzig, and J. Lippincott-Schwartz. A contractile and counterbalancing adhesion system controls the 3D shape of crawling cells. *J. Cell Biol.*, 205:83–96, 2014.

[36] F. Jülicher, K. Kruse, J. Prost, and J.-F. Joanny. Active behavior of the cytoskeleton. *Phys. Rep.*, 449:3–28, 2007.

[37] P. F. Machado, J. Duque, J. Étienne, A. Martinez-Arias, G. B. Blanchard, and N. Gorfinkiel. Emergent material properties of developing epithelial tissues. *BMC Biol.*, 13:98, 2015.

[38] J. Étienne and A. Duperray. Initial dynamics of cell spreading are governed by dissipation in the actin cortex. *Biophys. J.*, 101(3):611–622, 2011.

[39] X. He and M. Dembo. On the mechanics of the first cleavage division of the sea urchin egg. *Exp. Cell Res.*, 233:252–273, 1997.

[40] K. Kruse, J.F. Joanny, F. Jülicher, J. Prost, and K. Sekimoto. Generic theory of active polar gels: a paradigm for cytoskeletal dynamics. *Eur. Phys. J. E*, 16:5–16, 2005.

[41] L. Trichet, J. Le Digabel, R. J. Hawkins, S. R. K. Vedula, M. Gupta, C. Ribrault, P. Hersen, R. Voituriez, and B. Ladoux. Evidence of a large-scale mechanosensing mechanism for cellular adaptation to substrate stiffness. *Proc. Natl. Acad. Sci. USA*, 109:6933–6938, 2012.

[42] P. Marcq, N. Yoshinaga, and J. Prost. Rigidity sensing explained by active matter theory. *Biophys. J.*, 101:L33–L35, 2011.

[43] P. Recho and L. Truskinovsky. An asymmetry between pushing and pulling for crawling cells. *Phys. Rev. E*, 87:022720, 2013.

[44] D. Ambrosi and A. Zanzottera. Mechanics and polarity in cell motility. *Physica D*, 2016.

[45] P. Recho and L. Truskinovsky. Maximum velocity of self-propulsion for an active segment. *Math. Mech. Solids*, 21:263–278, 2015.

[46] P. Recho, T. Putelat, and L. Truskinovsky. Contraction-driven cell motility. *Phys. Rev. Lett.*, 111:108102, 2013.

[47] O. M. Rossier, N. Gauthier, N. Biais, W. Vonnegut, M.-A. Fardin, P. Avigan, E. R. Heller, A. Mathur, S. Ghassemi, M. S. Koeckert, J. C. Hone, and M. P. Sheetz. Force generated by actomyosin contraction builds bridges between adhesive contacts. *EMBO J.*, 29:1033–1044, 2010.

[48] J. Étienne, A. Asnacios, D. Mitrossilis, V. Peschetola, and C. Verdier. How the cell got its shape : A visco-elasto-active model of the cytoskeleton. In *Congrès Français de Mécanique*, Besançon, France, September 2011. 6 pages.

[49] J. Étienne, E. J. Hinch, and J. Li. A Lagrangian–Eulerian approach for the numerical simulation of free-surface flow of a viscoelastic material. *J. Non-Newtonian Fluid Mech.*, 136:157–166, 2006.

[50] W.S. Rasband. Imagej. Technical report, U. S. National Institutes of Health, Bethesda, Maryland, USA, 2003–2014.

[51] D. Ambrosi, A. Duperray, V. Peschetola, and C. Verdier. Traction patterns of tumor cells. *J. Math. Biol.*, 58:163–181, 2009.

[52] R. Michel, V. Peschetola, B. Bedessem, J. Étienne, D. Ambrosi, A. Duperray, and C. Verdier. Inverse problems for the determination of traction forces by cells on a substrate: a comparison of two methods. *Comput. Methods Biomech. Biomed. Eng.*, 15:27–29, 2012. Congrès européen de biomécanique, Toulouse, 16-19 octobre 2012.

[53] R. Michel, V. Peschetola, J. Étienne, A. Duperray, G. Vitale, D. Ambrosi, L. Preziosi, and C. Verdier. Mathematical framework for traction force microscopy. *ESAIM Proc.*, 42:61–83, 2013.

[54] Y.-C. Lin, Dhananjay T. Tambe, C. Young Park, M. R. Wasserman, X. Trepat, R. Krishnan, G. Lenormand, J. J. Fredberg, and J. P. Butler. Mechanosensing of substrate thickness. *Phys. Rev. E*, 82:041918, 2010.

A Solution procedure for the one-dimensional model

We recall the problem in its dimensional form:

$$\begin{cases} -c_f v + \partial_x \sigma = 0 & \text{in } (-L, L) \\ \tau_\alpha \dot{\sigma} - 2\tau_\alpha \sigma \partial_x v + \sigma = \tau_\alpha G \partial_x v + \sigma_{\mathrm{a}} & \text{in } (-L, L) \\ \sigma = 0 & \text{at } x = \pm L \end{cases}$$

Here we have grouped the bulk and shear viscosity terms, without loss of generality in 1D.

A.1 Viscous limit

Assume $\tau_\alpha \ll 1$, but $\tau_\alpha G$ of order 1. In an interval of $[-L, L]$ with a constant c_f, we get

$$L_f^2 \partial_{xx} v - v = 0$$

with $L_f = \sqrt{\frac{\tau_\alpha G}{c_f}}$, thus $v = -U_0 \sinh \frac{x}{L_f} + U_1 \cosh \frac{x}{L_f}$.

If c_f is constant on $[-L, L]$, $U_1 = 0$ by symmetry and $\sigma = \sigma_{\mathrm{a}} \left(1 - \frac{\cosh \frac{x}{L_f}}{\cosh \frac{L}{L_f}} \right)$, thus $V_0 = \frac{L_f \sigma_{\mathrm{a}}}{\tau_\alpha G \cosh \frac{L}{L_f}}$. These solutions are reported in figure 3*b* and figure 3*c*.

If $c_f = c_f^0$ for $|v| < v^*$ and $c_f = c_f^1$ for $|v| > v^*$, call $x^* > 0$ the point at which the increasing function v is such that $v(x^*) = -v^*$. Then if $v^* < \frac{L_f \sigma_{\mathrm{a}}}{\tau_\alpha G \cosh \frac{L}{L_f}}$, we have $x^* < L$, and on the interval $[x^*, L]$ we have:

$$v_{|_{[x^*,L]}} = -v^* \cosh \frac{\xi(x - x^*)}{L_f} + \left(v^* \sinh \frac{\xi(L - x^*)}{L_f} - \sigma_{\mathrm{a}} \frac{L_f}{\tau_\alpha G \xi} \right) \frac{\sinh \frac{\xi(x - x^*)}{L_f}}{\cosh \frac{\xi(L - x^*)}{L_f}}$$

and

$$v_{|_{[0,x^*]}} = -v^* \sinh \frac{\xi(x - x^*)}{L_f}$$

with $\xi = \sqrt{c_f^1 c_f^0}$.

We can prescribe v^* by imposing the continuity of stress at x^*, which is equivalent in 1D to impose the continuity of the derivative of v, we find :

$$v^* = \frac{L_f \sigma_{\mathrm{a}}}{\tau_\alpha G} \frac{\sinh \frac{x^*}{L_f}}{\xi \sinh \frac{x^*}{L_f} \sinh \frac{\xi(L - x^*)}{L_f} + \cosh \frac{x^*}{L_f} \cosh \frac{\xi(L - x^*)}{L_f}}$$

Notation	Meaning, measured or calculated value
α, β	Any index among x and y
$\dot{\boldsymbol{\varepsilon}}$	Rate-of-strain tensor
κ	Two-dimensional Lamé's first coefficient
	No experimental data
$\Omega^{3\mathrm{D}}$	Space occupied by cell
Ω_c	Projection of $\Omega^{3\mathrm{D}}$ on plane (x, y)
Ω_c^i	Same, specifying frame number i
Ω	Field of view containg Ω^c
τ_α	Relaxation time of actomyosin
	$\tau_\alpha \simeq 10^3$ s [21]
c_f	Effective friction coefficient
c_f^0	Friction coefficient where $\lvert \boldsymbol{v} \rvert \ll v^*$
c_f^1	Friction coefficient where $\lvert \boldsymbol{v} \rvert \gg v^*$
D	Typical diameter of cell
	$D = 40$ to 100 µm in experiments
	Distances nondimensionalised by $D = 50$ µm
G	Two-dimensional shear modulus
h	Height of cell
	$h/D \lesssim 0.1$, $\partial_\alpha h \lesssim 0.1$
$\boldsymbol{n}$	External normal to Ω_c in (x, y) plane
T	Characteristic time of actomyosin retrograde flow
	$T = 10^3$ to 10^4 s [21]
Nondimensional model parameters	
λ	Second viscosity, $\lambda = \kappa/G$
	Taken equal to 1 (arbitrary)
$\boldsymbol{\sigma}_\mathrm{a} = \sigma_\mathrm{a} \boldsymbol{I}$	Myosin-generated 2D pre-stress [21]
	Nondimensionalised by $\tau_\alpha G/T = 5$ kPa·µm from experiments
	Found to be of the order of 30, i.e. 150 kPa·µm
ζ	Velocity-dependent friction coefficient
	Nondimensionalised by $\tau_\alpha G/D^2 = 10$ kPa·s·µm^{-1}
ζ_0	Friction coefficient ζ where $v \ll v^*$
	Found to be of the order of 20, i.e. 200 kPa·s·µm^{-1}.
ζ_1	Friction coefficient where $v \gg v^*$
	Found to vary around 5, i.e. 50 kPa·s·µm^{-1}.
v^*	Critical velocity (phenomenological parameter)
	Found to vary around 0.1, i.e. 10^{-3} µm·s^{-1}.
De	Deborah number
	De $= \tau_\alpha/T \lesssim 1$ from experiments
	Taken from 0 to 1 in 1D solutions, 0 in 2D simulations
Nondimensional model unknowns	
$\boldsymbol{\sigma}$	Two-dimensional stress tensor
	Nondimensionalised by $\tau_\alpha G/T = 5$ kPa·µm from experiments
$\boldsymbol{v}$	Field of actomyosin velocity in plane (x, y)
	Nondimensionalised by $D/T \simeq 10^{-2}$ µm/s
$\boldsymbol{T}$	Field of traction
	Nondimensionalised by $\tau_\alpha G/(TD) = 100$ Pa from experiments

Table 1: Parameters and variables reference list.

This result is shown in supplementary figure **??**

If now we want to prescribe v^* rather than x^*, we can identify the desired value by numerical inversion, as v^* is strictly monotonic in x^*, see supplementary figure **??**.

A.2 Full viscoelastic model

In permanent regime, $\dot{\sigma} = v \partial_x \sigma$, thus the system to solve is:

$$\begin{aligned} \partial_x v &= \frac{\tau_\alpha c_f v^2 + \sigma - \sigma_\mathrm{a}}{\eta + 2\tau_\alpha \sigma} \\ \partial_x \sigma &= c_f v \end{aligned}$$

There is no known analytical solution to this system in general, we resort to numerical integration using Octave software in order to approximate its solution.

Results are shown in supplementary figure **??**. The purely viscous approximation matches closely the solution of the visco-elastic problem for De $\lesssim 0.1$, and is still a fair approximation for De and up to 1.

B Two-dimensional problem

B.1 Variational formulation

In this section we detail how the problem is transformed into the variational form. Following the 1D results, we take $De = 0$. With the hypothesis that substrate deformation rate is small, $\tilde{\dot{\boldsymbol{\varepsilon}}} = \boldsymbol{D}(\boldsymbol{v})$, which is the symmetrical part of the tensor $\boldsymbol{\nabla}(\boldsymbol{v})$. So equations 4 become, dropping the $\tilde{\ }$ symbol:

$$-\boldsymbol{\nabla} \cdot \boldsymbol{\sigma} + \zeta \boldsymbol{v} = 0, \tag{8}$$

with $\boldsymbol{\sigma} = \lambda \mathrm{tr}\,(\boldsymbol{D}(\boldsymbol{v}))\boldsymbol{I} + 2\boldsymbol{D}(\boldsymbol{v}) + \boldsymbol{\sigma}_\mathrm{a}$, where we have denoted $\lambda = \kappa / G$.

Then, we multiply the first equation by an arbitrarily test-function $\boldsymbol{w} \in W = H^1(\Omega_\mathrm{c})^2$ and we integrate over Ω_c:

$$\int_{\Omega_\mathrm{c}} -(\boldsymbol{\nabla} \cdot \boldsymbol{\sigma}) \cdot \boldsymbol{w} \,\mathrm{d}x = \int_{\Omega_\mathrm{c}} -\zeta \boldsymbol{v} \cdot \boldsymbol{w} \,\mathrm{d}x, \qquad \forall \boldsymbol{w} \in W$$

Using Green's formula, we can write:

$$\int_{\Omega_\mathrm{c}} (\boldsymbol{\nabla} \cdot \boldsymbol{\sigma}) \cdot \boldsymbol{w} \,\mathrm{d}x + \int_{\Omega_\mathrm{c}} \boldsymbol{\sigma} : \boldsymbol{D}(\boldsymbol{w}) \,\mathrm{d}x = \int_{\partial\Omega_\mathrm{c}} \boldsymbol{\sigma} : (\boldsymbol{w} \otimes \boldsymbol{n}) \,\mathrm{d}s$$

Remark that on $\partial\Omega_\mathrm{c}$, $\boldsymbol{\sigma} : (\boldsymbol{w} \otimes \boldsymbol{n}) = (\boldsymbol{\sigma}\boldsymbol{n}) \cdot \boldsymbol{w}$ which is equal to zero due to the boundary condition $\boldsymbol{\sigma}(\boldsymbol{v}) \cdot \boldsymbol{n} = 0$. So the integral over $\partial\Omega_\mathrm{c}$ is zero and the problem rewrites:

$$\int_{\Omega_\mathrm{c}} \boldsymbol{\sigma}(\boldsymbol{v}) : \boldsymbol{D}(\boldsymbol{w}) \,\mathrm{d}x = \int_{\Omega_\mathrm{c}} \zeta \boldsymbol{v} \cdot \boldsymbol{w} \,\mathrm{d}x$$

From the constitutive equation, we have:

$$\begin{aligned}\boldsymbol{\sigma}(\boldsymbol{v}) : \boldsymbol{D}(\boldsymbol{w}) &= \lambda \mathrm{tr}\,(\boldsymbol{D}(\boldsymbol{v}))(I : \boldsymbol{D}(\boldsymbol{w})) + 2\boldsymbol{D}(\boldsymbol{v}) : \boldsymbol{D}(\boldsymbol{w}) + \boldsymbol{\sigma}_{\mathrm{a}} : \boldsymbol{D}(\boldsymbol{w}) \\ &= \lambda \mathrm{tr}\,(\boldsymbol{D}(\boldsymbol{v}))\boldsymbol{\nabla} \cdot \boldsymbol{w} + 2\boldsymbol{D}(\boldsymbol{v}) : \boldsymbol{D}(\boldsymbol{w}) + \boldsymbol{\sigma}_{\mathrm{a}} : \boldsymbol{D}(\boldsymbol{w})\end{aligned}$$

For now, we assume that the myosin pre-stress $\boldsymbol{\sigma}_{\mathrm{a}}$ is isotropic, thus $\boldsymbol{\sigma}_{\mathrm{a}} = \sigma_{\mathrm{a}}\boldsymbol{I}$. Then we finally have the variational formulation of the problem:

$$\begin{aligned}&\int_{\Omega_{\mathrm{c}}} \lambda \mathrm{tr}\,(\boldsymbol{D}(\boldsymbol{v})) \cdot \boldsymbol{\nabla} \cdot \boldsymbol{w}\,\mathrm{d}x \\ &\quad + \int_{\Omega_{\mathrm{c}}} 2\boldsymbol{D}(\boldsymbol{v}) : \boldsymbol{D}(\boldsymbol{w})\,\mathrm{d}x \\ &\qquad + \int_{\Omega_{\mathrm{c}}} \zeta \boldsymbol{v} \cdot \boldsymbol{w}\,\mathrm{d}x = -\sigma_{\mathrm{a}} \int_{\Omega_{\mathrm{c}}} \boldsymbol{\nabla} \cdot \boldsymbol{w}\,\mathrm{d}x \qquad \forall \boldsymbol{w} \in W. \qquad (9)\end{aligned}$$

Next we define the finite element space $W_h = \{\boldsymbol{w}_h \in W, w_h|_{K\in\mathcal{T}^i_{\mathrm{c},h}} \in P_2(K)\}$. The friction field ζ_h is calculated from a previous guess $\boldsymbol{v}_h^{k-1}$ as stated in the main text, and we solve equation (**??**) for $\boldsymbol{v}_h^k$ in W_h using test functions $\boldsymbol{w}_h \in W_h$ using the finite element library Rheolef.

B.2 Fitting of the myosin pre-stress parameter σ_{a}

From the solution of the 1D problem in the viscous case, we see that the myosin pre-stress σ_{a} appears as a multiplying factor of the solution. This is convenient in terms of data fitting, since this allows to calculate the traction field $\boldsymbol{T}_1$ for a unit choice of $\sigma_{\mathrm{a}} = \sigma_{\mathrm{a}}^1$, and then to minimise explicitly the difference between $\boldsymbol{T}_1$ and $\boldsymbol{T}_{\mathrm{exp}}$. Here is the precise derivation of this result.

Let $\boldsymbol{v}_1$ be solution of the problem:

$$\zeta_{v^*}(|\boldsymbol{v}|)\boldsymbol{v} - \lambda \boldsymbol{\nabla} \cdot \boldsymbol{v} - \boldsymbol{\nabla} \cdot 2\boldsymbol{D}(\boldsymbol{v}) = 0 \quad \text{on } \partial\Omega_{\mathrm{c}} \qquad (10a)$$

with $v^* = v_1^*$ and the boundary condition:

$$\boldsymbol{D}(\boldsymbol{v}_1)\boldsymbol{n} = -\sigma_{\mathrm{a}}^1 \boldsymbol{n} \quad \text{on } \partial\Omega_{\mathrm{c}} \qquad (10b)$$

Then by plugging $\boldsymbol{v}_1 = \frac{\sigma_{\mathrm{a}}^1}{\sigma_{\mathrm{a}}^2}\boldsymbol{v}_2$ in equation (**??**), we get:

$$\zeta_{v_1^*}\left(\frac{\sigma_{\mathrm{a}}^1}{\sigma_{\mathrm{a}}^2}|\boldsymbol{v}_2|\right)\boldsymbol{v}_2 - \boldsymbol{\nabla} \cdot 2\eta \boldsymbol{D}(\boldsymbol{v}_2) = 0 \quad \text{on } \partial\Omega_{\mathrm{c}}$$

and thus $\boldsymbol{v}_2$ is solution of equation (**??**) with $v^* = v_2^* = \frac{\sigma_{\mathrm{a}}^2}{\sigma_{\mathrm{a}}^1}\boldsymbol{v}_1^*$ and the boundary condition:

$$\boldsymbol{D}(\boldsymbol{v}_2)\boldsymbol{n} = -\sigma_{\mathrm{a}}^2 \boldsymbol{n} \quad \text{on } \partial\Omega_{\mathrm{c}}$$

if and only if the choice of the friction law is scale invariant, i.e. $\zeta_{\lambda v^*}(\lambda|\boldsymbol{v}|) = \zeta_{v^*}(|\boldsymbol{v}|)$.

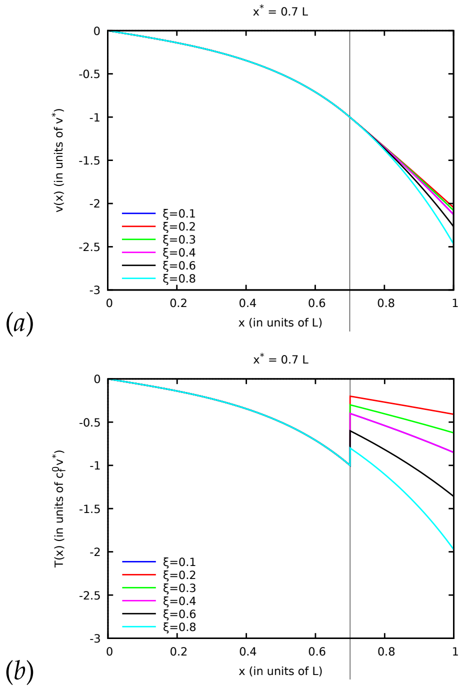

Figure S1: (*a*) Actin velocity and (*b*) traction forces for various values of $\xi = \sqrt{c_f^1/c_f^0}$, see supplementary text **??**

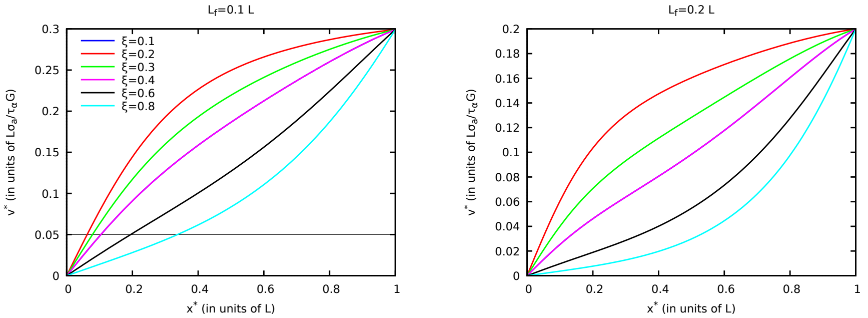

Figure S2: Determination of the position x^* such that $v(x^*) = v^*$: plots of the threshold velocity v^* corresponding to solutions obtained with given parameters L_f and ξ and choice of x^*, see supplementary text **??**.

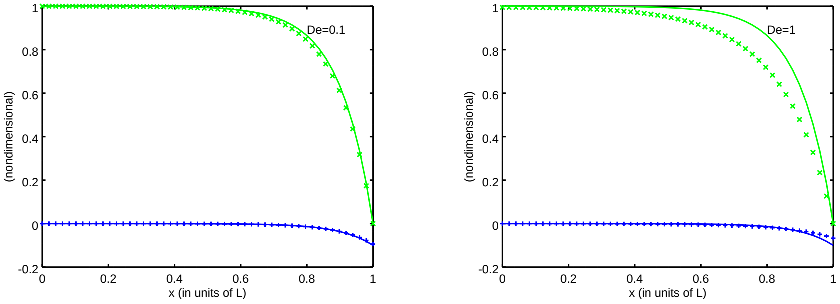

(*a*) (*b*)

Figure S3: Comparison of results with the full visco-elastic model equation (5) with the solution in the viscous limit De $= 0$, for two values of the Deborah number. Green '×' symbols, stress σ, blue '+' symbols, velocity v, see supplementary text **??**.

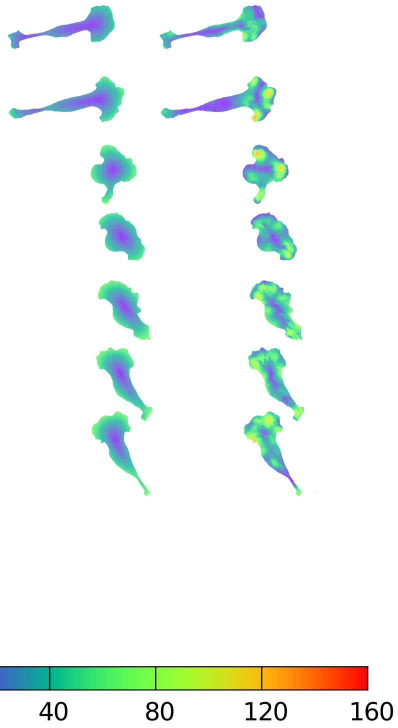

Figure S4: Comparison of intensity of traction field predicted by the model (left) and calculated from experimental observations (right) during a migration experiment of T24 cell number 2, instants shown are $t = 0$, 8, 16, 24, 32, 40 and 48 min. Magnitudes are given in Pascals.

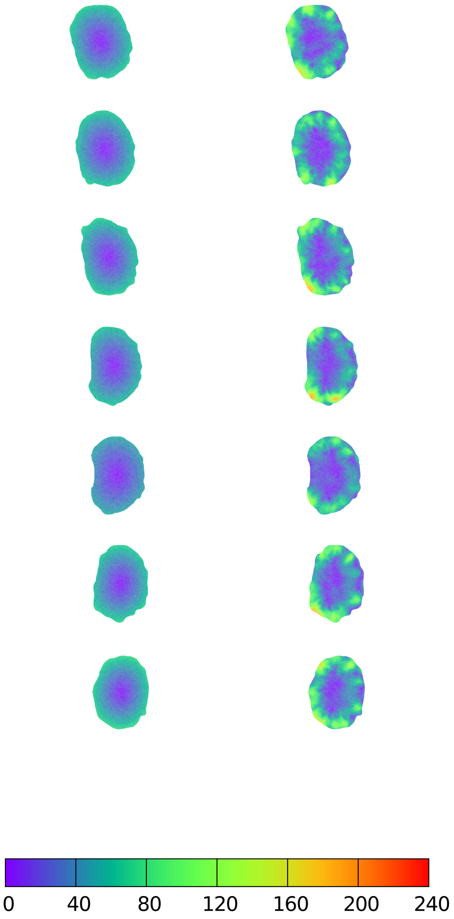

Figure S5: Comparison of intensity of traction field predicted by the model (left) and calculated from experimental observations (right) during a migration experiment of an RT112 cell, instants shown are $t = 0$, 12, 24, 36 48 60 and 72 min ($t = 0$ is also show in figure 4*b*) The RT112 morphology is much simpler and does not change in the course of migration. The model predicts a centripetal traction field which globally agrees with observations throughout migration. The same shortcomings of the model as for the lamella region in T24 cells, figure 4*a*, are noted. Here no parameter is adjusted, ζ_0 and σ_a are taken to the value chosen for T24 cell experiment at $t = 0$, figure 4*a*. Magnitudes are given in Pascals.